JOURNAL OF SYNCHROTRON RADIATION
ISSN 1600-5775

Hard X-ray phase-contrast tomography of non-homogeneous specimens: grating interferometry *versus* propagation-based imaging

Maite Ruiz-Yaniz,[a,b]* Irene Zanette,[b,c] Adrian Sarapata,[b] Lorenz Birnbacher,[b] Mathias Marschner,[b] Michael Chabior,[b] Margie Olbinado,[a] Franz Pfeiffer[b] and Alexander Rack[a]

[a]European Synchrotron Radiation Facility, 71 Rue des Martyrs, 38000 Grenoble, France, [b]Lehrstuhl für Biomedizinische Physik, Physik-Department and Institut für Medizintechnik, Technische Universität München, James-Franck-Strasse 1, 85748 Garching, Germany, and [c]Diamond Light Source, Harwell Science and Innovation Campus, Didcot OX11 0DE, UK. *Correspondence e-mail: maite.ruiz@tum.de

Received 18 November 2015
Accepted 7 June 2016

Edited by A. Momose, Tohoku University, Japan

Keywords: phase contrast; X-ray micro-tomography; phase retrieval; X-ray imaging.

X-ray phase-contrast imaging is an effective approach to drastically increase the contrast and sensitivity of microtomographic techniques. Numerous approaches to depict the real part of the complex-valued refractive index of a specimen are nowadays available. A comparative study using experimental data from grating-based interferometry and propagation-based phase contrast combined with single-distance phase retrieval applied to a non-homogeneous sample is presented (acquired at beamline ID19-ESRF). It is shown that grating-based interferometry can handle density gradients in a superior manner. The study underlines the complementarity of the two techniques for practical applications.

1. Introduction

Computed tomography (CT) with high spatial resolution in the micrometer range (frequently also termed micro-tomography or μCT) is an established technique for probing the interior of a specimen in a widely non-destructive way. Nowadays, by using laboratory-based sources, μCT can be applied in a routine manner similar to visible-light microscopy or electron microscopy. The use of microtomography has proven to be beneficial in diverse scientific fields such as materials research, biology, paleontology, non-destructive evaluation or cultural heritage (Bonse & Busch, 1996; Stock, 2008; Banhart, 2008; Maire & Withers, 2014).

While the early development efforts of μCT were concentrated on increasing the achievable spatial resolution, more recently the driver for new applications and instrumentation is the quest for high contrast and/or sensitivity (Flannery *et al.*, 1987; Koch *et al.*, 1998; Banhart, 2008). Exploiting δ, the real part of the complex-valued index of refraction, for imaging is a popular approach to increasing the imaging sensitivity, frequently termed also as phase-contrast imaging (Nugent, 2010; Mayo *et al.*, 2012). Progressing from data representing the local-density-related attenuation behavior of a specimen towards depicting its local refraction allows for drastically increasing sensitivity in X-ray imaging, since δ is several orders of magnitude larger than the imaginary part β (absorption) of the refractive index, especially for low-Z materials (Snigirev *et al.*, 1995; Cloetens *et al.*, 1996; Wilkins *et al.*, 1996).

In general, heterogeneous samples present to some extent a challenge for X-ray imaging. For example, in medical CT

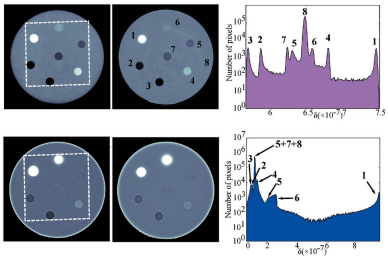

metal implants in bone can lead to artifacts (Hsieh, 2003). Due to the increased sensitivity of phase-contrast X-ray imaging, tomography of heterogeneous specimens is affected as well. Being able, for example, to apply propagation-based phase-contrast imaging in combination with phase retrieval to specimens containing a mixture of polymers and metals is under development (Langer *et al.*, 2012). Studying soft and hard tissues in one specimen is possible but requires dedicated protocols (Beltran *et al.*, 2010, 2011; Holme *et al.*, 2014). Hence, a careful consideration of the suitability of phase-contrast techniques for specimens showing density gradients is needed.

Different X-ray techniques have been developed to depict the real part of the refractive index of a specimen such as analyzer-based imaging (Förster *et al.*, 1980), crystal-based interferometry (Bonse & Hart, 1965), propagation-based phase-contrast imaging (PBI) in combination with so-called phase retrieval (Cloetens *et al.*, 1999), imaging using coded apertures (Munro *et al.*, 2012), or grating-based interferometry (XGI) (David *et al.*, 2002; Momose *et al.*, 2003; Weitkamp *et al.*, 2005; Pfeiffer *et al.*, 2008).

Although nowadays μCT with phase contrast can be applied using laboratory sources, XGI and especially PBI for example with applicable exposure time are still preferably performed with bright X-ray sources at synchrotron radiation facilities. In this article we shall compare two popular phase-contrast imaging techniques commonly used in combination with synchrotron light sources and their ability to image specimens with varying density profiles: PBI in combination with subsequent phase-retrieval processing *versus* XGI.

Both techniques are known to be highly suited to studying soft-tissue samples in a complementary manner, *i.e.* rather homogeneous samples: PBI methods offer higher spatial resolution, while XGI gives superior density contrast (Zanette *et al.*, 2013*a*; Lang *et al.*, 2014). But soft-tissue specimens are not representative of the large variety of samples commonly investigated with phase-contrast imaging. In particular, for example, specimens from materials research are often heterogeneous. Knowledge on performance and limitations of both techniques to depict the interior of specimens with density gradients, especially in a comparative manner, is missing. With respect to the available literature, this comparative study will therefore concentrate on the density aspect while a comparative analysis of the spatial resolving power of both techniques is omitted. For the sake of simplicity, this work is performed under sufficient photon flux. The potentials of the two approaches are compared under the conditions at beamline ID19 at the European Synchrotron Radiation Facility (ESRF; Grenoble, France). Furthermore, practical aspects of implementing phase-contrast techniques at a synchrotron radiation beamline will be discussed.

2. Methods

In this article we focus on presenting experimental data depicting the performance of two popular phase-contrast imaging approaches to handle specimens with density gradients.

2.1. Propagation-based phase-contrast imaging

The principle layout of an experiment to perform PBI at a synchrotron light source is sketched in Fig. 1(*a*): by leaving a drift-space between sample and detector and using a (partially) coherent illumination, interfaces within the sample are made visible by an interference fringe pattern created downstream of the sample. The latter is related to the refraction of the wavefront on the object interfaces which gives edge-enhanced images (Snigirev *et al.*, 1995; Cloetens *et al.*, 1996). The creation of the fringes depends strongly on, among others, the experimental parameters, such as the propagation distance and the photon energy. Consequently, the propagation distance needs to be adapted for a given photon energy and effective detector pixel size in order to maximize the contrast (Willmott, 2011; Zabler *et al.*, 2005; Weitkamp *et al.*, 2011). Under the assumption of a fully transparent object the recorded fringe-images can be interpreted as the Laplacian of the phase of the wavefront after passing the sample (Bremmer, 1952). Hence, phase-retrieval techniques need to be applied to those images in order to

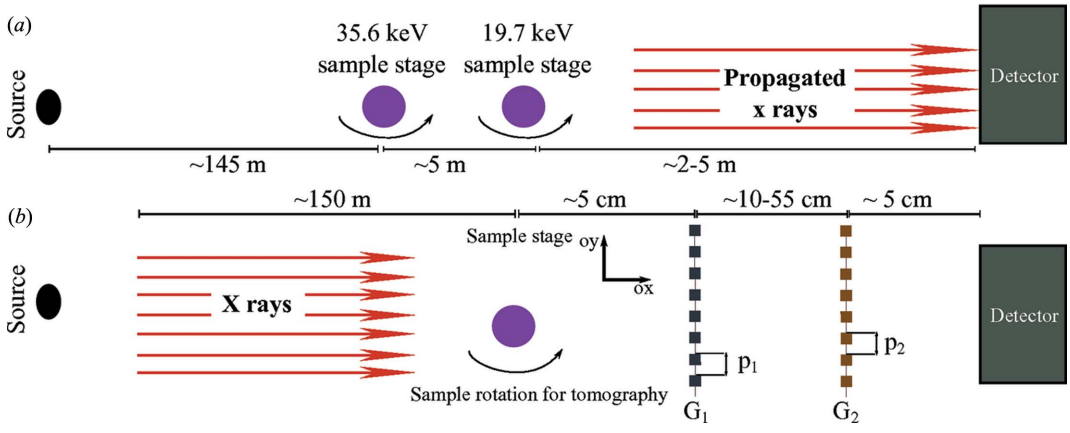

Figure 1
(*a*) Schematic representation of the propagation-based (PBI) setup at ID19. (*b*) Schematic representation of the grating interferometer (XGI) installation at ID19.

establish a direct correlation between the material a voxel represents and its associated grey-value. Various approaches have been introduced in recent years to perform phase retrieval on propagation-based phase-contrast images (*cf.* Langer *et al.*, 2008). In this study the method proposed by Paganin *et al.* (2002) is used, which resolves the transport-of-intensity equation assuming a homogeneous sample as well as monochromaticity and a flat or only mildly curved wavefront. In practice it has been found, however, that the approach can deliver excellent results even if the former assumptions are violated, *i.e.* polychromatic illumination and to some extent non-homogeneous samples (Myers *et al.*, 2007; Weitkamp *et al.*, 2011). Nowadays Paganin's phase-retrieval algorithm is used, for example, at beamline ID19 of the ESRF in a routine manner (Mirone *et al.*, 2014). It is easily applicable, robust and yields excellent results with samples requiring phase contrast but for which knowing the internal morphology is mainly relevant, *i.e.* it is not necessarily applied in a quantitative manner (Pierce *et al.*, 2013; Sanchez *et al.*, 2012; Bayerlein *et al.*, 2014).

Propagation-based phase-contrast imaging is very attractive for synchrotron radiation sources as basically it can be used with the same protocol as for absorption-based μCT: the only difference is the propagation distance between the sample and the detector which needs to be extended. Hence, PBI with or without phase retrieval is applied at numerous beamlines around the globe (Banhart, 2008). It remains challenging to use coarse spatial resolution: the large pixel sizes lead to long propagation distances of up to several meters which are not easily available on every beamline (Pagot *et al.*, 2005; Weitkamp *et al.*, 2011).

2.2. Grating interferometry

XGI is an imaging technique that was developed in the early 2000s (David *et al.*, 2002; Momose *et al.*, 2003). It provides simultaneously three inherently registered signals: absorption, phase and dark-field signal (Weitkamp *et al.*, 2005; Pfeiffer *et al.*, 2008). It is a quantitative imaging technique that is very sensitive to small density variations, being able to differentiate density differences down to 0.5 mg cm^{-3} (Zanette *et al.*, 2013*b*). Furthermore, it can also be implemented with laboratory X-ray sources (Pfeiffer *et al.*, 2006). All these reasons make XGI a versatile technique that is being used in many different applications such as medical imaging or material sciences (Schulz *et al.*, 2012; Yaroshenko *et al.*, 2013; Herzen *et al.*, 2014; Sarapata *et al.*, 2015; Grandl *et al.*, 2015).

The interferometer used in this study is composed of two gratings, *cf.* Fig. 1(*b*). The phase grating (G1) introduces a phase shift to the incoming X-rays. Through the Talbot effect (Talbot, 1836), after traversing the grating a periodic intensity modulation is created with maximum intensity variations at the so-called fractional Talbot distances (Cloetens *et al.*, 1997). Because the period of the intensity modulation is too small (∼2–5 μm) to be directly detected with a detector with a large field of view as desired, a second grating G2 is used to analyze this pattern. From this analysis the first derivative of the phase of the wavefront after passing the sample is retrieved in the direction perpendicular to the grating lines. Integration in Fourier space, for example, combined with the tomographic reconstruction algorithm can be applied in order to recover the phase information in three dimensions (Pfeiffer *et al.*, 2007).

Compared with propagation-based phase-contrast imaging, grating-based interferometry enables a more compact experimental setup and offers tri-modal contrast images with a single scan. Especially for coarse spatial resolutions, *i.e.* large pixel sizes, the mentioned long-propagation distances of several meters as for PBI are not required. These advantages are compromised by the fact that specific X-ray optical elements, *i.e.* the gratings, as well as a more sophisticated data acquisition protocol are required.

3. Experiments

The experiments were performed at the ID19 hard X-ray imaging beamline (ESRF). ID19 is a long beamline with the experimental hutch placed 145 m away from the X-ray source, providing a partially coherent X-ray beam suitable for performing phase-contrast imaging with high sensitivity. For the study, standard configurations of ID19 were chosen. Hence, the two phase-contrast modalities are compared under conditions relevant to daily operation at ESRF.

As an X-ray source, the single-harmonic undulator U17.6 was used. This study was carried out at two photon energies: 19.7 keV and 35.6 keV. In both cases, the filtered 'pink' beam from the undulator was used without any monochromator. The 19.7 keV 'pink' beam was obtained with 0.7 mm-thick Al filter, a 1 mm diamond filter, an undulator gap set to 30 mm and had an energy bandwidth of 1.35 keV at its full width at half-maximum (FWHM) (photon flux density of around 5×10^{10} photons s^{-1} mm^{-2}). The 35.6 keV beam energy configuration was obtained with an undultor gap of 15 mm, introducing 5.6 mm-thick Al and 0.14 mm-thick Cu filters and it had an energy bandwidth of 6.1 keV at its FWHM (photon flux density of around 2×10^{11} photons s^{-1} mm^{-2}). The detector was an indirect system consisting of a 10 μm-thick gadolinium oxysulfide scintillator (Gd_2O_2S), a magnifying lens system, and a FReLon CCD camera with 2048 × 2048 pixels (Douissard *et al.*, 2012; Labiche *et al.*, 2007). The measurements using grating interferometry were made using the FReLon E2V with an effective pixel size of 8 μm. The propagation-based images were acquired using a FReLon 2K with an effective pixel size of 7.5 μm.

Fig. 1(*a*) shows a schematic representation of the propagation-based setup used for this experiment. Two different configurations were used for the measurements. At 19.7 keV, the sample was placed 2.6 m upstream of the detector. For the second configuration using X-rays at 35.6 keV, the sample was placed 8.1 m upstream of the detector.

A schematic representation of the interferometer position in the experimental hutch can be seen in Fig. 1(*b*). At a photon energy of E = 19.7 keV, a 4.8 μm-period G1 made of Si with a structure height of 23 μm was used (creating approximately π

shift). G2 had a period of 2.4 μm and was made of Au, with a structure height of 100 μm. The inter-grating distance was set to 48.5 cm, matching the 11th Talbot distance. For the second configuration, a phase grating G1 with a period of 4.8 μm and a height of 44 μm was used, which created a π shift to X-rays of 35 keV. The same G2 from the 19.7 keV configuration was used. The inter-grating distance used was 41.5 cm, matching the fifth Talbot distance.

3.1. Sample

The sample measured in this study was a phantom composed of eight different materials, listed in Table 1. The phantom was designed for phase measurements with high sensitivity, with all the rod material density differences with respect to the base material ranging between 0.047 and 0.237 g cm^{-3}. The phantom had a cylindrical form, with a diameter of 12 mm and was 20 mm long. Each of the rods inside had a 1 mm diameter and was 20 mm long.

3.2. Measurements

For a fair comparison of XGI and PBI, as similar experimental configurations as possible were used for each photon energy. However, one should notice that, due to the difference in the experimental setups of each technique, it was not possible to equal the flux and the exposure time of the scans.

XGI measurements were performed using the phase-stepping method, in which the phase grating is moved in the direction perpendicular to the grating lines and the optical axis at least over one period of the absorption grating in five evenly spaced steps. During this movement several images are recorded, and the phase-stepping curve is obtained for each pixel (Weitkamp *et al.*, 2005). For the XGI measurements at 19.7 keV, the exposure time per frame was 1 s while for the measurements at 35.6 keV the exposure time per frame was 0.2 s. For tomography, phase stepping scans were performed at 1499 evenly spaced angular views of the sample over 360°. The resulting total exposure time was 125 min for the configuration at 19.6 keV and 25 min for the configuration at 35.6 keV.

For the PBI measurements one single projection was acquired per angle; 2000 projections in total over 180° were acquired. In the two energy configurations the exposure time per frame was set to 0.3 s, which yielded a total exposure time of 10 min. The total exposure time in the measurements using propagation-based imaging is considerably shorter in comparison with the XGI measurements.

The reconstruction of the PBI data was carried out applying Paganin's phase-retrieval algorithm (Paganin *et al.*, 2002) together with the filtered back-projection algorithm and standard image restoration protocols. For this purpose the ESRF software *High Speed Tomography in Python* (*PyHST*) was used (Mirone *et al.*, 2014). For the PBI reconstructions three different δ/β values close to the theoretical values of the materials in the phantom were used for the two energy configurations. For the theoretical δ values the Windt database (Windt, 1998) and for the δ/β the CXRO database was used (Henke *et al.*, 1993).

Table 1
Material composition of the phantom's inserts.

Material	Density (g cm^{-3})
1 Polyvinyl chloride (PVC)	1.36
2 Polyamide/nylon (PA)	1.00
3 Polyethilene (PE)	0.95
4 Polymethylmethacrylate PMMA	1.19
5 Polyurethane (PUR) + carbone	1.09
6 Epoxy resin (EP) + iodine	1.16
7 Polyurethane	1.08
8 Epoxy resin (EP)	1.13

The reconstruction of the XGI data is carried out in two steps. First a pixelwise Fourier analysis is performed in order to extract the different signals out of the phase-stepping curves. Once the absorption or differential-phase projections are reconstructed, the same filtered back-projection algorithm used to reconstruct the PBI slices is used. In order to reconstruct the phase a Hilbert filter is used, which enables the integration of the differential projections in Fourier space (Pfeiffer *et al.*, 2007).

4. Results

In order to compare the performance of PBI and XGI methods, a slice of each reconstructed volume of δ is shown in Fig. 2. To best visualize the images, all the phantom slices are shown on a scale range of 80 times the standard deviation of the background, calculated in a region of interest (ROI) of 46 × 56 pixels. The slices of tomography reconstructions from PBI measurements using three different δ/β values are shown in Figs. 2(*d*), 2(*g*) and 2(*j*). When the δ/β value chosen is close to one of the materials in the phantom, the image of this material is expected to be shown sharp and homogeneous. On the other hand, when the δ/β value differs from the one corresponding to the material, the shape of the rod becomes blurred and no longer homogeneous. In principle, they are more sophisticated approaches which could perform single-distance phase retrieval on such a phantom sample with spatially well defined constituents in a superior manner (Beltran *et al.*, 2010). However, commonly they are less frequently used compared with the original approach by Paganin *et al.* (Weitkamp *et al.*, 2011).

At 19.7 keV (see Fig. 2*d*) one can see that the δ/β value of 300 is not suited for all the materials in the sample. This value was chosen as closest to the theoretical δ/β of PVC (material 1), which is 242. However, in the reconstruction the rod does not appear homogeneous, because it is surrounded by an unknown material which can be clearly seen in in Fig. 2(*b*) and might have a very different δ/β value. When increasing the δ/β value to 2000, we become closer to the theoretical values corresponding to PMMA (material 4) and PA (material 2), *i.e.* 2301 and 2337, respectively. As we can see in Fig. 2(*g*), the rods look more homogeneous than the ones corresponding to the rest of the materials. When reconstructing the slice using a δ/β of 3000, we see that PE (material 3) becomes more homo-

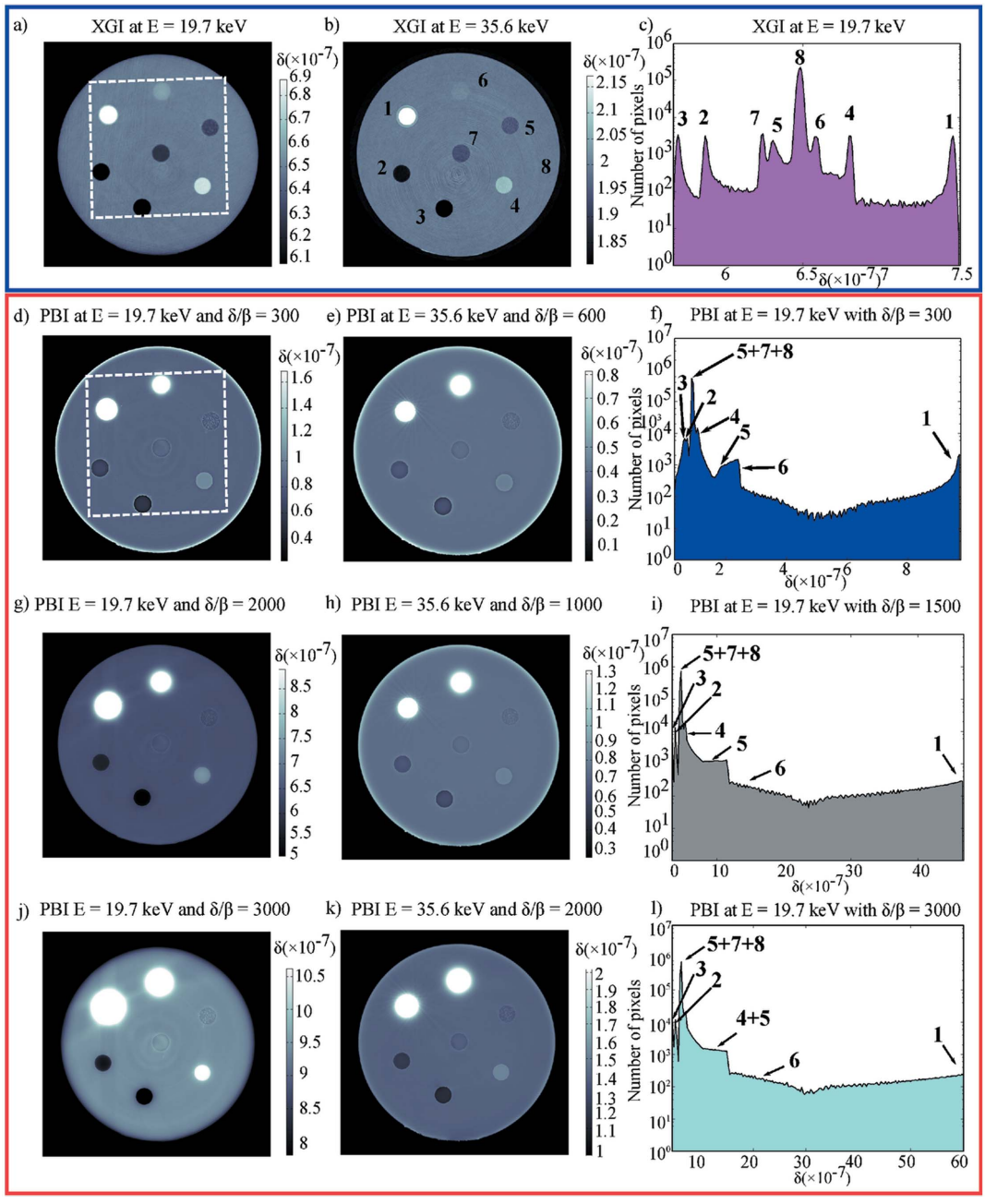

Figure 2
Comparison of XGI and PBI results at two X-ray photon energies. The results of the XGI measurements are shown inside the blue rectangle, and the PBI results are shown inside the red rectangle. (*a*) XGI phase-slice at 19.7 keV; the white dashed rectangle shows the ROI used for calculating the histogram in (*c*). (*b*) XGI phase-slice at 35.6 keV; the numbers correspond to the different materials of Table 1. (*c*) Histogram of the XGI slice at 19.7 keV on logarithmic scale, over a region only containing materials inside the phantom. Inside the red rectangle the results of the PBI measurements are shown. (*d*), (*g*), (*j*) PBI slices at 19.7 keV using δ/β values of 300, 2000 and 3000, respectively. (*e*), (*h*), (*k*) PBI slices at 35.6 keV using δ/β values of 600, 1000 and 2000, respectively. (*f*), (*i*), (*l*) Corresponding histograms of the PBI slices at 19.7 keV on a logarithmic scale.

geneous. This is because the corresponding theoretical value is 3272.

Three exemplary δ/β values are shown in this article. When δ/β values higher than 3000 are chosen (not shown in this article), PVC and EP-I (materials 1 and 6) become more sharp and homogeneous, and the rest of the phantom materials become indistinguishable in this gray scale range.

The slice of tomography reconstruction from the XGI measurement at 19.7 keV is shown in Fig. 2(*a*). In this case, all eight materials are clearly visible, sharp and each rod looks homogeneous.

For a better understanding of the difference in the quality of the images obtained with the two techniques, a histogram of the data acquired at 19.7 keV is also shown in Figs. 2(*c*), 2(*f*), 2(*i*) and 2(*l*). The histograms have been computed in the rectangular ROI shown by the white dashed line in Figs. 2(*a*) and 2(*d*), in order to avoid the background. If the technique provides enough sensitivity to separate all the materials in the

phantom, the pixels in each of the materials should produce a distinct peak in the histogram.

For the histograms of the phase slices obtained using PBI at 19.7 keV, all the peaks are close to each other. Eventually, the pixel values corresponding to several materials are all together in one and the same peak, which makes the differentiation difficult or even impossible. This shows the limitation of PBI in depicting δ of a specimen with a moderate density gradient between 0.047 and 0.237 g cm^{-3}.

All four histograms of the PBI measurements show a similar behavior. In all four cases the highest peak is composed of pixel values of materials 5, 7 and 8. Note that material 5 is a heterogeneous mixture of polymethilmethacrylate (PUR) and carbon. Carbon has a higher δ value than PUR and can be distinguished between the peaks of material numbers 6 and 4 or together with material 4. Pixel values of materials 2 and 3, although separated, are very close to each other.

When looking at the XGI histogram in Fig. 2(*c*), all the materials are clearly distinguishable. XGI allows the quantitative measurement of δ. A ROI of 50 × 50 pixels is selected in the material and mean values are calculated. The error is calculated taking into account the standard deviation of the ROI and the error of the inter-grating distance. For example, the theoretical δ of PVC at 19.7 keV is 7.47×10^{-7}, the calculated mean value of the experimental GI results at 19.7 keV gives a value of $7.46 \times 10^{-7} \pm 0.02$. For PMMA the measured value at 19.7 keV, $6.80 \times 10^{-7} \pm 0.01$, slightly deviates from the expected theoretical value of 6.87×10^{-7}. The deviation can be the result of the effect of the energy bandwidth of the X-ray beam. The bandwidth of 1.35 keV corresponds to a δ of 0.95×10^{-7}. The high sensitivity of XGI on density variations is visible, since even material number 6 [epoxy resin (EP) + iodine], with a mass density difference of 4% with respect to the base material, can be clearly distinguished.

One should note the difference in values of materials 4 (PMMA) and 6 (EP + iodine) using PBI and XGI. At 19.7 keV photon energy PMMA has a theoretical δ value of 6.94×10^{-7}, EP has a theoretical δ value of 5.9×10^{-7} and iodine has a theoretical δ value of 21.9×10^{-7}. Material 6 is a mixture of EP and iodine. In the measurements using PBI the mixture peak appears at a higher value than that of the PMMA. Contrarily, the measured δ of the PMMA in the XGI measurements is higher than that of the mixture. This can be related to the highly attenuating nature of iodine which will make region 6 appear denser and brighter in the tomographic slice than other materials: the phase-retrieval by Paganin *et al.* reconstructs an effective thickness for a given refractive index. The XGI image of δ will not show this difference in β. The latter is related to the so-called attenuating image of XGI (data not shown here).

Table 2
Contrast-to-noise ratios of seven different materials with respect to the base material for the four different configurations analyzed in the study.

Material numbers	CNR XGI (E = 19.7 keV)	CNR XGI (E = 35.6 keV)	CNR PBI (E = 19.7 keV, δ/β = 300)	CNR PBI (E = 35.6 keV, δ/β = 600)
1–8	84.5	30.9	13.7	84
2–8	50.4	21.5	20.0	20.1
3–8	68.8	14.7	36.4	26.0
4–8	24.0	9.8	22.8	19.3
5–8	8.2	3.2	0.1	0.1
6–8	9.5	2.5	22.7	84.3
7–8	22.7	4.8	0.7	0.2

Regarding the results with respect to the X-ray energy, contrast-to-noise ratios were calculated between materials 1–7 and the base material 8 according to (Herzen *et al.*, 2009):

$$\mathrm{CNR} = \frac{|\, S_A - S_B \,|}{\left(\sigma_A^2 + \sigma_B^2\right)^{1/2}}, \qquad (1)$$

where S_A and S_B are the mean δ values of two different materials and σ_A and σ_B are the corresponding standard deviations calculated in a ROI of 50 × 50 pixels. Results of this calculation can be seen in Table 2. They refer to standard configurations in use at beamline ID19 (ESRF), *i.e.* they are more of an indicator but cannot serve as absolute measure to compare the potentials of the two approaches.

Slices obtained from PBI show that the highest photon energy configuration gives better contrast-to-noise ratios. This behavior is related to the dependency on the δ/β ratio chosen for the reconstruction. At higher photon energies the difference between δ and β becomes smaller, and the δ/β constant assumption is better fulfilled. On the other hand, XGI results show better contrast-to-noise ratios at 19.7 keV. This is probably because the differences between δ of the different materials are stronger at lower X-ray energies.

At 19.7 keV, XGI results in a higher contrast-to-noise ratio for every material pair except for material number 6. This is the mixture of iodine and EP and the one with the lowest density difference with respect to the base material: again, the highly attenuating iodine will be beneficial for the contrast in PBI due to the phase-retrieval approach used. At 35.6 keV, PBI gives a better contrast-to-noise ratio for the material pairs 1–8, 3–8, 4–8 and 6–8.

One has to mention that the dose to the sample has been significantly higher for the XGI scans than for the PBI scans, *cf.* the total exposure times per scan mentioned in §3.2. Hence, the applied XGI protocol might be more desirable for non-biological specimens.

5. Discussion

When using the above detailed experimental settings at beamline ID19, XGI gives better contrast-to-noise ratios at the lower X-ray energy. Contrarily, PBI shows better contrast-to-noise ratios when higher photon energy is applied. This is

related to the fact that δ and β values for the different constituents of the sample become closer with increasing photon energy. Therefore, at the higher photon energy configuration the variation of the δ/β ratio throughout the phantom matches better the assumption of being constant.

The choice between the two phase-contrast techniques is not trivial as several more technical constraints at a synchrotron beamline need to be considered as well. Assuming that the required gratings for XGI are nowadays widely commercially available, a rather compact XGI setup can be realised even for more coarse spatial resolutions. The demands of the technique in terms of coherence properties of the incoming wavefront are somewhat relaxed with respect to PBI while access to high spatial resolution, especially below 1 µm, is limited (Lang *et al.*, 2014). As mentioned several times, the data acquisition protocol and post-processing for XGI remains more complex. This limits, as well, access to higher temporal resolution, *i.e.* to acquire tomographic scans within a few seconds or less (Rack *et al.*, 2010). Different XGI acquisition schemes have been demonstrated in recent years which potentially can shorten the exposure times (Zanette *et al.*, 2012).

Contrarily, PBI does not require additional optical elements: the same protocol as for microtomography in absorption mode is used, with only the sample-detector distance increased. This rather simple acquisition protocol makes PBI somewhat robust and gives access to higher temporal resolution (Rack *et al.*, 2010). PBI with coarser spatial resolution and/or higher photon energies depends on the layout of a synchrotron beamline as propagation distances of more than 10 m can be required (Pagot *et al.*, 2005; Weitkamp *et al.*, 2010, 2011; Tromba *et al.*, 2010; MacDowell *et al.*, 2012; Rack *et al.*, 2008, 2009; Stampanoni *et al.*, 2007; Rau *et al.*, 2011). For data processing and contrary to XGI, *a priori* information, *i.e.* the refractive index in terms of δ and β, is needed, available either from existing databases or can be determined by a guess-and-check approach. As outlined within this article, density gradients within the sample remain a challenge for PBI in combination with single-distance phase retrieval. For specimens with substantially stronger density gradients than used in this study it is common to apply a δ/β value for the lighter material while the denser material remains with a fringe (*cf.* for example Artioli *et al.*, 2012): the fringe-related contrast in such cases is frequently substantially weaker than the attenuation contrast.

6. Summary

We have presented an experimental study of X-ray grating interferometry and propagation-based phase-contrast imaging in terms of their capability of handling heterogeneous specimens with moderate density gradients. A comparison of the X-ray phase-tomography data obtained using XGI and PBI shows the superiority of XGI to PBI with respect to the mentioned density gradients: the XGI pictures maintain a high sharpness while for PBI in combination with single-distance phase retrieval a substantial blur of the images remains. These underline the robustness of XGI as well as its ability to characterize a sample in a quantitative manner while the PBI approach combined with single-distance phase retrieval is not able to handle density gradients as low as 4%. Hence, it could be desirable for the future to further evaluate the potential of XGI for application fields outside the biomedical community, *i.e.* materials research or cultural heritage.

Acknowledgements

We wish to thank QRM GmbH for manufacturing of the phantom. The authors gratefully acknowledge Jürgen Mohr from the Karlsruhe Institute of Technology and Christian David from Paul Scherrer Institut for fabricating the gratings. We thank one of the anonymous reviewers who substantially improved the quality of this manuscript with numerous detailed comments. FP acknowledges financial support through the DFG Cluster of Excellence Munich-Center for Advanced Photonics (DFG EXC-158) and the European Research Council (ERC, H2020, AdG 695045).

References

Artioli, G., Dalconi, M. C., Parisatto, M., Valentini, L., Voltolini, M. & Ferrari, G. (2012). *Int. J. Mater. Res.* (Formerly *Z. Metallkdd.*), **103**, 145–150.
Banhart, J. (2008). Editor. *Advanced Tomographic Methods in Materials Research and Engineering*. Oxford University Press.
Bayerlein, B., Zaslansky, P., Dauphin, Y., Rack, A., Fratzl, P. & Zlotnikov, I. (2014). *Nat. Mater.* **13**, 1102–1107.
Beltran, M. A., Paganin, D. M., Siu, K. K. W., Fouras, A., Hooper, S. B., Reser, D. H. & Kitchen, M. J. (2011). *Phys. Med. Biol.* **56**, 7353–7369.
Beltran, M., Paganin, D., Uesugi, K. & Kitchen, M. (2010). *Opt. Express*, **18**, 6423–6436.
Bonse, U. & Busch, F. (1996). *Prog. Biophys. Mol. Biol.* **65**, 133–169.
Bonse, U. & Hart, M. (1965). *Appl. Phys. Lett.* **6**, 155–156.
Bremmer, H. (1952). *Physica*, **18**, 469–485.
Cloetens, P., Barrett, R., Baruchel, J., Guigay, J.-P. & Schlenker, M. (1996). *J. Phys. D*, **29**, 133–146.
Cloetens, P., Guigay, J. P., De Martino, C., Baruchel, J. & Schlenker, M. (1997). *Opt. Lett.* **22**, 1059–1061.
Cloetens, P., Ludwig, W., Baruchel, J., Van Dyck, D., Van Landuyt, J., Guigay, J. P. & Schlenker, M. (1999). *Appl. Phys. Lett.* **75**, 2912–2914.
David, C., Nöhammer, B., Solak, H. H. & Ziegler, E. (2002). *Appl. Phys. Lett.* **81**, 3287–3289.
Douissard, P.-A., Cecilia, A., Rochet, X., Chapel, X., Martin, T., van de Kamp, T., Helfen, L., Baumbach, T., Luquot, L., Xiao, X., Meinhardt, J. & Rack, A. (2012). *J. Instrum.* **7**, P09016.
Flannery, B. P., Deckman, H. W., Roberge, W. G. & D'Amico, K. L. (1987). *Science*, **237**, 1439–1444.
Förster, E., Goetz, K. & Zaumseil, P. (1980). *Krist. Techn.* **15**, 937–945.
Grandl, S., Scherer, K., Sztrókay-Gaul, A., Birnbacher, L., Willer, K., Chabior, M., Herzen, J., Mayr, D., Auweter, S. D., Pfeiffer, F., Bamberg, F. & Hellerhoff, K. (2015). *Eur. Radiol.* **25**, 3659–3668.
Henke, B., Gullikson, E. & Davis, J. (1993). *At. Data Nucl. Data Tables*, **54**, 181–342.
Herzen, J., Donath, T., Pfeiffer, F., Bunk, O., Padeste, C., Beckmann, F., Schreyer, A. & David, C. (2009). *Opt. Express*, **17**, 10010–10018.
Herzen, J., Willner, M. S., Fingerle, A. A., Noël, P. B., Köhler, T., Drecoll, E., Rummeny, E. J. & Pfeiffer, F. (2014). *PLos ONE*, **9**, e83369.

Holme, M. N., Schulz, G., Deyhle, H., Weitkamp, T., Beckmann, F., Lobrinus, J. A., Rikhtegar, F., Kurtcuoglu, V., Zanette, I., Saxer, T. & Müller, B. (2014). *Nat. Protoc.* **9**, 1401–1415.
Hsieh, J. (2003). *Computed Tomography: Principles, Design, Artifacts and Recent Advances*, Vol. 114. Bellingham: SPIE Press.
Koch, A., Raven, C., Spanne, P. & Snigirev, A. (1998). *J. Opt. Soc. Am. A*, **15**, 1940–1951.
Labiche, J.-C., Mathon, O., Pascarelli, S., Newton, M. A., Ferre, G. G., Curfs, C., Vaughan, G., Homs, A. & Carreiras, D. F. (2007). *Rev. Sci. Instrum.* **78**, 091301.
Lang, S., Zanette, I., Dominietto, M., Langer, M., Rack, A., Schulz, G., Le Duc, G., David, C., Mohr, J., Pfeiffer, F., Müller, B. & Weitkamp, T. (2014). *J. Appl. Phys.* **116**, 154903.
Langer, M., Cloetens, P., Guigay, J.-P. & Peyrin, F. (2008). *Med. Phys.* **35**, 4556–4566.
Langer, M., Cloetens, P., Pacureanu, A. & Peyrin, F. (2012). *Opt. Lett.* **37**, 2151–2153.
MacDowell, A. A., Parkinson, D. Y., Haboub, A., Schaible, E., Nasiatka, J. R., Yee, C. A., Jameson, J. R., Ajo-Franklin, J. B., Brodersen, C. R. & McElrone, A. J. (2012). *Proc. SPIE*, **8506**, 850618.
Maire, E. & Withers, P. (2014). *Int. Mater. Rev.* **59**, 1–43.
Mayo, S. C., Stevenson, A. W. & Wilkins, S. W. (2012). *Materials*, **5**, 937.
Mirone, A., Brun, E., Gouillart, E., Tafforeau, P. & Kieffer, J. (2014). *Nucl. Instrum. Methods Phys. Res. B*, **324**, 41–48.
Momose, A., Kawamoto, S., Koyama, I., Hamaishi, Y., Takai, K. & Suzuki, Y. (2003). *Jpn. J. Appl. Phys.* **42**, L866–L868.
Munro, P. R. T., Ignatyev, K., Speller, R. D. & Olivo, A. (2012). *Proc. Natl Acad. Sci. USA*, **109**, 13922–13927.
Myers, G. R., Mayo, S. C., Gureyev, T. E., Paganin, D. M. & Wilkins, S. W. (2007). *Phys. Rev. A*, **76**, 045804.
Nugent, K. A. (2010). *Adv. Phys.* **59**, 1–99.
Paganin, D., Mayo, S. C., Gureyev, T. E., Miller, P. R. & Wilkins, S. W. (2002). *J. Microsc.* **206**, 33–40.
Pagot, E., Fiedler, S., Cloetens, P., Bravin, A., Coan, P., Fezzaa, K., Baruchel, J., Härtwig, J., von Smitten, K., Leidenius, M., Karjalainen-Lindsberg, M. L. & Keyriläinen, J. (2005). *Phys. Med. Biol.* **50**, 709–724.
Pfeiffer, F., Bech, M., Bunk, O., Kraft, P., Eikenberry, E. F., Brönnimann, C., Grünzweig, C. & David, C. (2008). *Nat. Mater.* **7**, 134–137.
Pfeiffer, F., Kottler, C., Bunk, O. & David, C. (2007). *Phys. Rev. Lett.* **98**, 108105.
Pfeiffer, F., Weitkamp, T., Bunk, O. & David, C. (2006). *Nat. Phys.* **2**, 258–261.
Pierce, S. E., Ahlberg, P. E., Hutchinson, J. R., Molnar, J. L., Sanchez, S., Tafforeau, P. & Clack, J. A. (2013). *Nature (London)*, **494**, 226–229.
Rack, A., García-Moreno, F., Schmitt, C., Betz, O., Cecilia, A., Ershov, A., Rack, T., Banhart, J. & Zabler, S. (2010). *J. X-ray Sci. Tech.* **18**, 429–441.
Rack, A., Weitkamp, T., Bauer Trabelsi, S., Modregger, P., Cecilia, A., dos Santos Rolo, T., Rack, T., Haas, D., Simon, R., Heldele, R., Schulz, M., Mayzel, B., Danilewsky, A. N., Waterstradt, T., Diete, W., Riesemeier, H., Müller, B. R. & Baumbach, T. (2009). *Nucl. Instrum. Methods Phys. Res. B*, **267**, 1978–1988.
Rack, A., Zabler, S., Müller, B., Riesemeier, H., Weidemann, G., Lange, A., Goebbels, J., Hentschel, M. & Görner, W. (2008). *Nucl. Instrum. Methods Phys. Res. A*, **586**, 327–344.
Rau, C., Wagner, U., Pešić, Z. & De Fanis, A. (2011). *Phys. Status Solidi A*, **208**, 2522–2525.
Sanchez, S., Ahlberg, P. E., Trinajstic, K. M., Mirone, A. & Tafforeau, P. (2012). *Microsc. Microanal.* **18**, 1095–1105.
Sarapata, A., Ruiz-Yaniz, M., Zanette, I., Rack, A., Pfeiffer, F. & Herzen, J. (2015). *Appl. Phys. Lett.* **106**, 154102.
Schulz, G., Waschkies, C., Pfeiffer, F., Zanette, I., Weitkamp, T., David, C. & Müller, B. (2012). *Sci. Rep.* **2**, 826.
Snigirev, A., Snigireva, I., Kohn, V., Kuznetsov, S. & Schelokov, I. (1995). *Rev. Sci. Instrum.* **66**, 5486–5492.
Stampanoni, M., Groso, A., Isenegger, A., Mikuljan, G., Chen, Q., Meister, D., Lange, M., Betemps, R., Henein, S. & Abela, R. (2007). *AIP Conf. Proc.*, **879**, 848–851.
Stock, S. R. (2008). *MicroComputed Tomography: Methodology and Applications*. Boca Raton: CRC Press.
Talbot, H. (1836). *Philos. Mag.* **9**, 401–407.
Tromba, G., Longo, R., Abrami, A., Arfelli, F., Astolfo, A., Bregant, P., Brun, F., Casarin, K., Chenda, V., Dreossi, D., Hola, M., Kaiser, J., Mancini, L., Menk, R. H., Quai, E., Quaia, E., Rigon, L., Rokvic, T., Sodini, N., Sanabor, D., Schultke, E., Tonutti, M., Vascotto, A., Zanconati, F., Cova, M., Castelli, E. & Siu, K. K. W. (2010). *AIP Conf. Proc.* **1266**, 18–23.
Weitkamp, T., Diaz, A., David, C., Pfeiffer, F., Stampanoni, M., Cloetens, P. & Ziegler, E. (2005). *Opt. Express*, **13**, 6296–6304.
Weitkamp, T., Haas, D., Wegrzynek, D. & Rack, A. (2011). *J. Synchrotron Rad.* **18**, 617–629.
Weitkamp, T., Tafforeau, P., Boller, E., Cloetens, P., Valade, J.-P., Bernard, P., Peyrin, F., Ludwig, W., Helfen, L., Baruchel, J., Denecke, M. & Walker, C. T. (2010). *AIP Conf. Proc.* **1221**, 33–38.
Wilkins, S. W., Gureyev, T. E., Gao, D., Pogany, A. & Stevenson, A. W. (1996). *Nature (London)*, **384**, 335–338.
Willmott, P. (2011). *An Introduction to Synchrotron Radiation*. Chichester: John Wiley and Sons.
Windt, D. L. (1998). *Comput. Phys.* **12**, 360–370.
Yaroshenko, A., Meinel, F. G., Bech, M., Tapfer, A., Velroyen, A., Schleede, S., Auweter, S., Bohla, A., Yildirim, A., Nikolaou, K., Bamberg, F., Eickelberg, O., Reiser, M. F. & Pfeiffer, F. (2013). *Radiology*, **269**, 427–433.
Zabler, S., Cloetens, P., Guigay, J.-P., Baruchel, J. & Schlenker, M. (2005). *Rev. Sci. Instrum.* **76**, 073705.
Zanette, I., Bech, M., Rack, A., Le Duc, G., Tafforeau, P., David, C., Mohr, J., Pfeiffer, F. & Weitkamp, T. (2012). *Proc. Natl Acad. Sci. USA*, **109**, 10199–10204.
Zanette, I., Lang, S., Rack, A., Dominietto, M., Langer, M., Pfeiffer, F., Weitkamp, T. & Müller, B. (2013*a*). *Appl. Phys. Lett.* **103**, 244105.
Zanette, I., Weitkamp, T., Leduc, G. & Pfeiffer, F. (2013*b*). *R. Soc. Chem. Adv.* **3**, 19816–19819.